THE ASTROPHYSICAL JOURNAL, 567:622–634, 2002 March 1

ENERGETIC PARTICLE OBSERVATIONS DURING THE 2000 JULY 14 SOLAR EVENT

JOHN W. BIEBER, WOLFGANG DRÖGE, PAUL A. EVENSON, AND ROGER PYLE
Bartol Research Institute, University of Delaware, Newark, DE 19716
DAVID RUFFOLO, UDOMSILP PINSOOK, PAISAN TOOPRAKAI, MANIT RUJIWARODOM, AND THIRANEE KHUMLUMLERT
Department of Physics, Chulalongkorn University, Thailand
AND
SÄM KRUCKER
Space Sciences Laboratory, University of California, Berkeley, CA 94720
Received 2001 July 10; accepted 2001 September 23

ABSTRACT

Data from nine high-latitude neutron monitors are used to deduce the intensity-time and anisotropy-time profiles and pitch-angle distributions of energetic protons near Earth during the major solar event on 2000 July 14 (also known as the Bastille Day event). In addition, particle and magnetic field measurements from *Wind*, the *Advanced Composition Explorer*, and the *Solar and Heliospheric Observatory* (*SOHO*) are used in the analysis. The observations are fitted with good agreement between two independent numerical models of interplanetary transport. The rapid decrease of anisotropy from a high initial value cannot be explained by a simple model of interplanetary transport. Hence, we invoke a barrier or magnetic bottleneck consistent with an observed magnetic disturbance from an earlier coronal mass ejection that was located ~ 0.3 AU beyond Earth's orbit at the time of the Bastille Day event. This work includes the first treatment of focused transport through a magnetic bottleneck. We conclude that the bottleneck reflected a major fraction ($\approx 85\%$) of the relativistic solar protons back toward Earth.

Subject heading: acceleration of particles — Sun: flares — Sun: particle emission

1. INTRODUCTION

Analysis and modeling of solar energetic particles provides vital information on particle scattering and transport in the interplanetary medium and on the acceleration and release of energetic particles near the Sun (Bieber, Evenson, & Pomerantz 1986; Beeck et al. 1987; Debrunner et al. 1988; Ruffolo 1991; Shea et al. 1991; Cramp et al. 1997; Dröge 2000a). The very large particle event of 2000 July 14, often called the "Bastille Day event" after the French holiday, affords an excellent opportunity to extend our knowledge of acceleration and transport processes in the heliosphere.

After 10:30 UT on 2000 July 14, solar cosmic rays were observed by the worldwide network of neutron monitors and by particle detectors on near-Earth spacecraft. The event was the largest in amplitude (at that time) since 1991 and was associated with a solar flare at 10:24 UT in NOAA region 9077 located at N22° W07°. It also registered in soft X-rays as a powerful X5-class eruption by the NOAA *GOES-8* satellite and as a full-halo coronal mass ejection (CME) observed with the C2 coronagraph on board the *Solar and Heliospheric Observatory* (*SOHO*) spacecraft. The CME drove an interplanetary shock wave that passed Earth about 15:00 UT on July 15 after a transit time of only ~ 28 hr, implying a mean speed of ~ 1500 km s^{-1}.

This work presents an analysis of solar energetic proton data acquired by a network of high-latitude neutron monitors and electron data acquired by the *Wind* spacecraft. The neutron monitor analysis employs only monitors with good directional sensitivity, and it uses a trajectory code to provide accurate geomagnetic corrections to the monitor viewing direction. Owing to these factors, we believe our analysis achieves unprecedented accuracy in determining the density and anisotropy of relativistic solar protons as a function of time through the event.

In order to determine the interplanetary scattering mean free path and solar injection profile, we model the proton and electron data using codes based upon the Boltzmann equation. A feature of the analysis is the use of two separate modeling approaches that were independently implemented by different subsets of the investigation team. The excellent consistency attained builds confidence in the validity of our conclusions.

Section 2 describes the analysis of neutron monitor data and also presents the *Wind* electron data. Section 3 describes our modeling efforts and the factors that led us to invoke a magnetic barrier beyond Earth as an important influence upon particle transport on Bastille Day 2000. Section 4 discusses the implications of our work and summarizes our conclusions.

2. OBSERVATIONS

2.1. *Relativistic Solar Protons*

2.1.1. *Overview of Data*

Figure 1 presents an overview of cosmic-ray activity around the time of the Bastille Day solar particle event.[1] A minor Forbush decrease early on July 10 was followed by a much larger decrease on July 13. (The latter decrease was associated with a solar event observed at 21:42 UT on July 10, as will be discussed in § 3.1.2.) As the larger decrease was in progress, relativistic solar particles arrived at Earth, causing a ground level enhancement (GLE) on Bastille Day (July 14). Finally, on July 15, yet another large Forbush decrease occurred. This decrease was caused by the CME associated with the Bastille Day GLE. The observations in Figure 1 were recorded by neutron monitors in Thule, Greenland, and McMurdo, Antarctica. We note that the

[1] The data shown in Figure 1 are available at http://www.bartol.udel.edu/~neutronm.

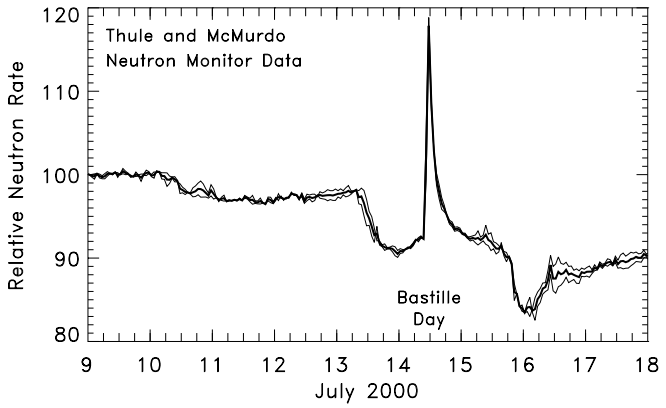

FIG. 1.—Cosmic-ray activity observed around the time of the Bastille Day (2000) solar particle event. Light lines show relative hourly count rates recorded by neutron monitors in Thule, Greenland, and McMurdo, Antarctica. The heavy line is their average. Each monitor was normalized to an index value of 100 on the first day plotted.

neutrons detected are secondary particles caused by nuclear interactions of cosmic rays with Earth's atmosphere. The primary cosmic rays initiating these interactions are predominantly protons.

Figure 2 provides a closer look at the GLE as seen by two high-latitude neutron monitors. At this time, the monitor in Thule, Greenland, was viewing particles arriving from a direction near the sunward Parker spiral (Fig. 4), while the monitor in Tixie Bay, Russia was viewing particles arriving from the opposite direction, away from the Sun. (Although Thule usually views toward the north, a combination of seasonal factors and time of day can combine to give it a midlatitude viewing direction, as happened for this event.) The two monitors have essentially identical energy responses. Therefore, the different traces in Figure 2 are caused by anisotropy of the solar cosmic rays. Because Thule was viewing toward the Sun, it observed an earlier onset, more rapid rise, and a higher peak intensity. Owing to scattering of particles in the solar wind, however, Tixie Bay also detected solar cosmic rays even though it was viewing away from the Sun. The ratio of count rates measured at Thule and Tixie is initially high (~ 7) but falls rapidly to a value slightly larger than unity.

Spectrum information for this event was obtained from a method that compares the count rate of the South Pole neutron monitor with the count rate of a nearby "Polar Bare" counter, which lacks the usual shielding of a standard NM64 detector system (Bieber & Evenson 1991). Results appear in Figure 3. As shown in the top panel, the Polar Bare is relatively more sensitive to low-energy primaries, and it records a higher percentage increase than the standard NM64 owing to the soft spectrum of solar cosmic rays. With the aid of yield functions provided by Stoker (1985), the ratio Bare/NM64 (*bottom panel*) can be translated into a

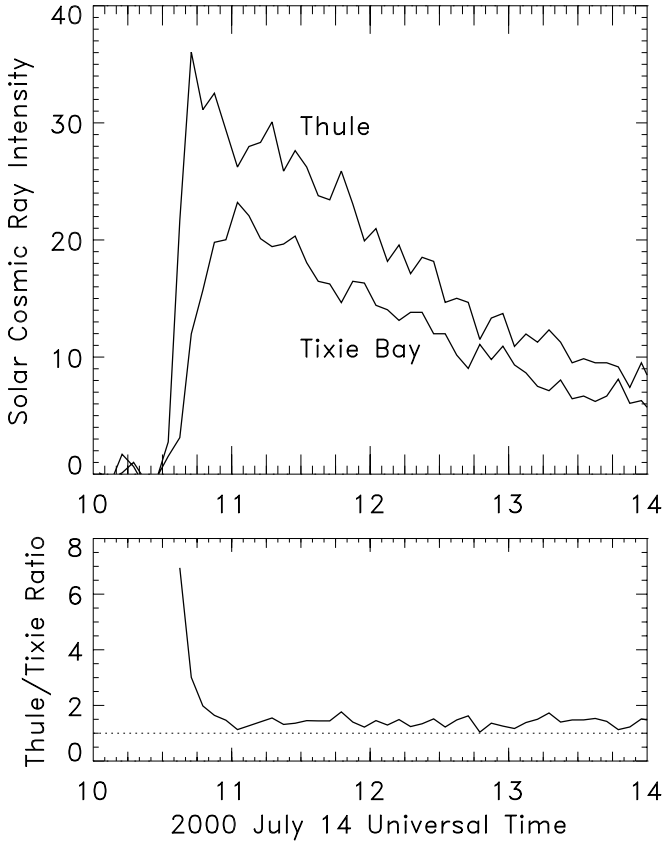

FIG. 2.—Time variation of solar cosmic-ray intensity measured by neutron monitors in Thule, Greenland, and Tixie Bay, Russia (*top*) plotted together with the ratio of intensities (*bottom*). The viewing directions of the two stations approximately represent the sunward (Thule) and antisunward (Tixie) Parker spiral direction. Intensity is expressed as a percentage increase over the preevent Galactic cosmic-ray background.

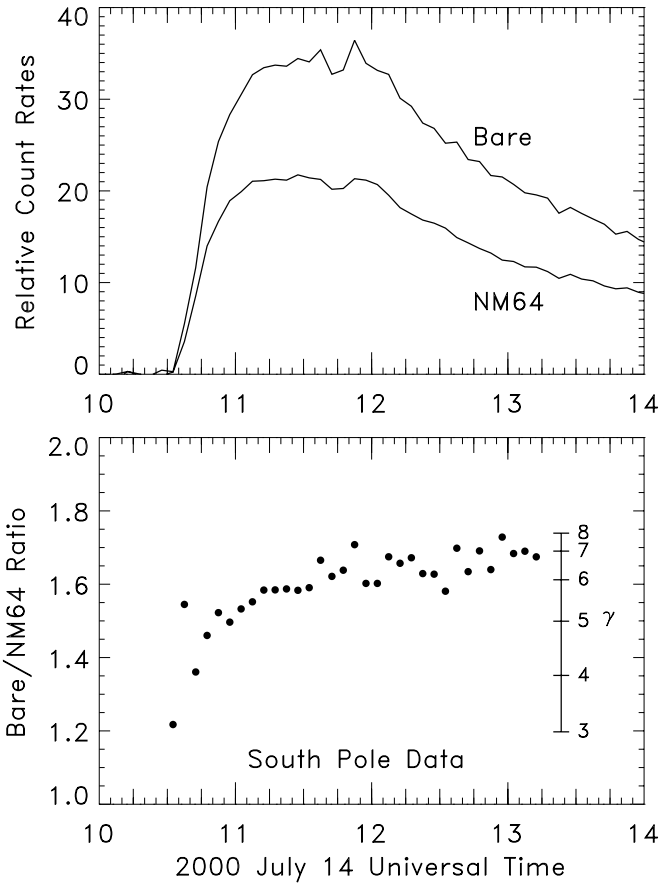

FIG. 3.—*Top:* Relative count rates recorded by a standard (NM64) neutron monitor at the South Pole and by a Polar Bare neutron counter that lacks the usual lead shielding. *Bottom:* Bare/NM64 ratio provides an indication of spectral index γ.

spectral index. We assume a differential rigidity spectrum of power-law form ($P^{-\gamma}$, with P the rigidity and γ the spectral index) with an upper cutoff at 20 GV. The scale on the right-hand side of the lower panel shows the spectral index implied by the corresponding Bare/NM64 ratio. We see that the spectrum gradually softened through the event. The spectral index was 4.9 averaged over the interval 10:35–11:00 UT, 5.9 over 11:00–12:00 UT, and 6.4 over 12:00–13:00 UT.

2.1.2. *Analysis Method*

To determine the density and anisotropy of this event as a function of time, data from nine high-latitude neutron monitors were employed. High-latitude monitors (those with geomagnetic cutoffs below about 1 GV) are preferred for this type of analysis for two reasons (Bieber & Evenson 1995). First, their cutoff is determined by atmospheric absorption rather than the geomagnetic cutoff. For this reason the monitors have essentially identical energy responses, and there is no need to disentangle spectrum effects from anisotropy effects. Any difference observed can generally be attributed to anisotropy alone. Second, the high-latitude monitors have excellent directional sensitivity. For a typical solar spectrum, the central 60% of particles detected arrive from a region spanning 50° or less.

Figure 4 displays the viewing directions of the neutron monitors used in this analysis at 10:30 UT on 2000 July 14. The solid dots show the viewing direction of the median (50th percentile) rigidity solar particle, which we estimate to be 2.2 GV. To characterize the spread of viewing directions with particle rigidity, we introduce the concept of percentile rigidities. To say that the 20th percentile rigidity is 1.3 GV, for instance, implies that 20% of the detected solar cosmic rays have rigidities below 1.3 GV. Percentile rigidities were computed for a solar particle spectrum varying inversely as rigidity to the fifth power, taking into account the monitor's energy response. As will become apparent, our conclusions rest heavily upon the evolution of particle intensities early in the event, when a spectral index of 5 is a reasonable choice according to Figure 3. (Choosing a spectral index of 6 would decrease the median rigidity of response from 2.2 GV to 1.5 GV. For stations used in this analysis, the viewing direction of the median rigidity would shift by 12° on average, and the median propagation speed would change by 8%. Owing to the small size of these shifts, we do not feel that use of a time-varying spectral index is required for this analysis.)

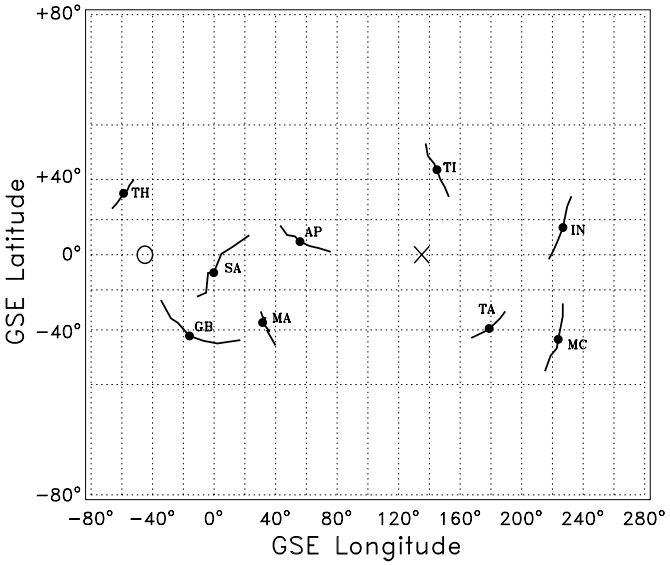

FIG. 4.—Viewing directions in GSE coordinates of the nine neutron monitors employed in this analysis. The solid circles show the viewing direction of the median rigidity solar cosmic ray, and the lines encompass the central 60% of the monitor energy response (see text). O and X designate the position of the nominal sunward and antisunward Parker spiral magnetic field. Station codes are the following: AP = Apatity, Russia; GB = Goose Bay, Canada; IN = Inuvik, Canada; MA = Mawson, Antarctica; MC = McMurdo, Antarctica; SA = Sanae, Antarctica; TH = Thule, Greenland; TA = Terre Adelie, Antarctica; and TI = Tixie Bay, Russia.

The line through each dot in Figure 4 spans viewing directions from the 20th percentile rigidity (1.3 GV) to the 80th percentile rigidity (3.8 GV). Thus the line encompasses the central 60% of the detector response to solar cosmic rays. Station viewing directions were computed with a trajectory code that takes into account Earth's magnetic field and magnetosphere (Lin, Bieber, & Evenson 1995).

Figure 4 shows that a 100° wide latitude band centered on the equatorial region is well sampled by the available stations. The situation contrasts with many spacecraft experiments, where the sensor aperture is fixed or a single sensor scans a plane. The figure also illustrates the good directional sensitivity of the high-latitude monitors. There is no overlap between stations for the central 60% of the monitor response.

Count rates from the stations were first corrected for atmospheric pressure variations using separate absorption lengths for Galactic and solar cosmic rays. Prior studies have generally found that the solar cosmic-ray absorption length is about 100 g cm^{-2} (Duggal 1979), and we adopted this value for our analysis. All stations were corrected to a common standard pressure of 760 mm Hg.

To take account of variations in detector efficiency, neutron monitors are typically calibrated "in flight" by normalizing stations to a common value during an interval prior to event onset. Ideally, the normalization interval should be a time when the Galactic cosmic rays are relatively quiet and nearly isotropic, thereby providing a standard calibration source. Because cosmic-ray anisotropies are strongly enhanced during Forbush decreases (Lockwood 1971; Duggal & Pomerantz 1976; Nagashima & Fujimoto 1993; Bieber & Evenson 1998), we decided to choose a normalization interval before the first of the Forbush decreases shown in Figure 1. Specifically, we used the 24 hr mean count rate on July 9. After the stations were normalized with respect to one another, background was subtracted using the Galactic background count rate observed from 10:00 to 10:30 UT on July 14, i.e., immediately before the GLE. Finally, the solar particle excess observed at each station was expressed as a percentage of this Galactic background.

Using our trajectory code, we computed asymptotic directions for each station as a function of time through the event. Data from the nine stations were fitted to a first-order anisotropy:

$$f(\theta, \phi) = n(1 + \xi_x \sin\theta \cos\phi + \xi_y \sin\theta \sin\phi + \xi_z \cos\theta)\,, \quad (1)$$

where f is the cosmic-ray intensity arriving from direction (θ, ϕ), n is the cosmic-ray density, ξ_x, ξ_y, ξ_z are the three

components of the anisotropy vector, θ is polar angle, and ϕ is azimuth. The anisotropy components as well as θ and ϕ are measured in geocentric solar ecliptic (GSE) coordinates. Longitude is equivalent to azimuth ϕ, and latitude is defined as $90° - \theta$.

To take into account the spread of viewing directions with rigidity (Fig. 4), we included 10 directions for each station in our fit, corresponding to the 5th, 15th, ... , 95th percentile rigidities. However, we found that this produced only small differences from the simple procedure of treating each station as a perfect unidirectional detector viewing the median rigidity direction. This demonstrates the advantage of high-latitude stations for studying particle anisotropies.

2.1.3. *Results*

Results of the analysis are displayed in Figure 5, which shows density, magnitude of anisotropy, and longitude and latitude of anisotropy. In the lower two panels a 1 hr centered moving average of the negative magnetic field direction determined from *Advanced Composition Explorer* (*ACE*) data is shown by the solid line. We used the negative of the field because Earth was in a region of "away" magnetic field at this time, and the negative field direction is more relevant for comparison with the particle anisotropy direction. (Note that we define anisotropy as the direction from which the particles are streaming, hence the anisotropy vector generally points toward the Sun.)

The density displays the characteristic rapid rise and slow decay of a solar particle event. The anisotropy is quite high initially, but rapidly decays to a low, comparatively steady level. For most of the time interval shown, the longitude of the anisotropy is near $\sim 330°$. This means the particles are flowing from the Sun, as expected. (Flow from the Sun along the 45° Parker spiral would correspond to a longitude of 315°.) Late in the time interval shown, the longitude and latitude points display considerable scatter. This happens because the anisotropy and density become small, and the direction of anisotropy cannot be precisely determined.

The longitude and latitude agree reasonably well with the measured magnetic field direction. It should be noted that a 2 GV proton has a Larmor radius of about 0.01 AU. A

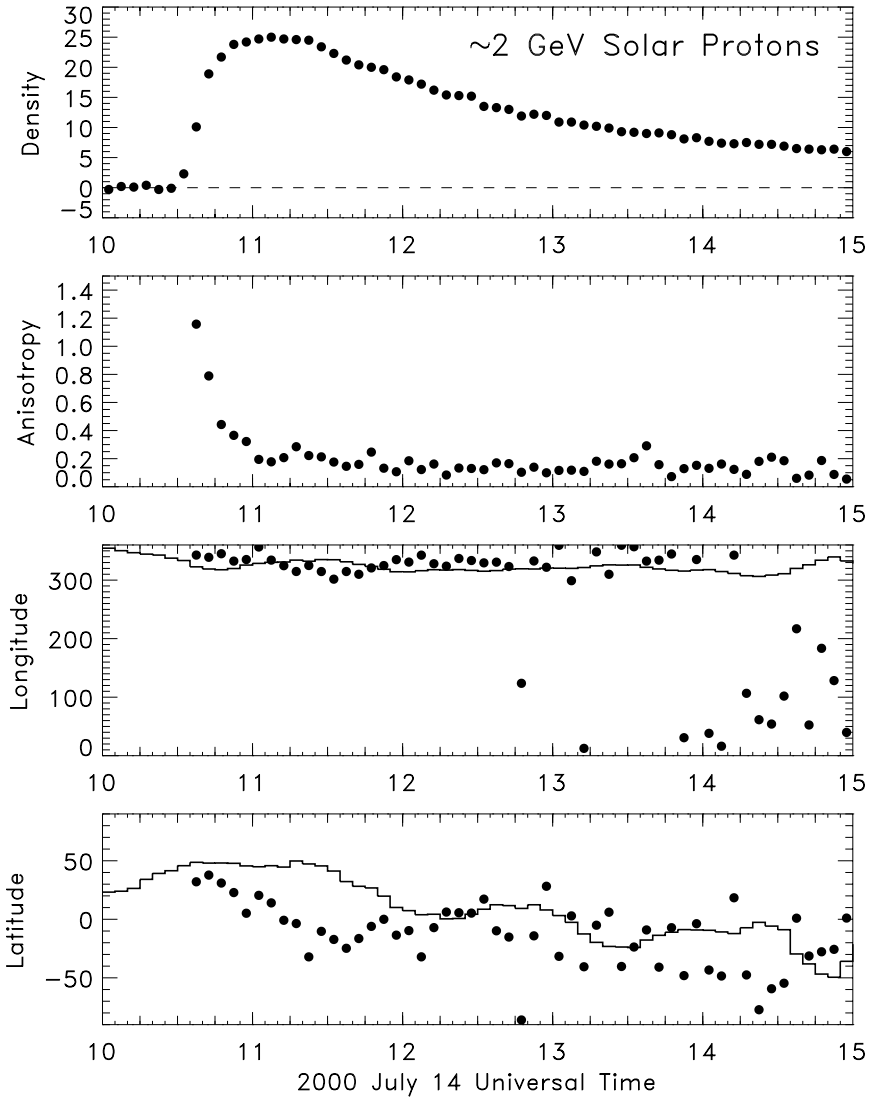

FIG. 5.—Results of fitting 5 minute average count rates from nine neutron monitors to a first-order anisotropy. Top to bottom are shown density, magnitude of anisotropy, GSE longitude of anisotropy, and GSE latitude of anisotropy. The lines in the lower two panels show the negative magnetic field direction measured aboard *ACE* (1 hr centered moving averages computed every 5 minutes).

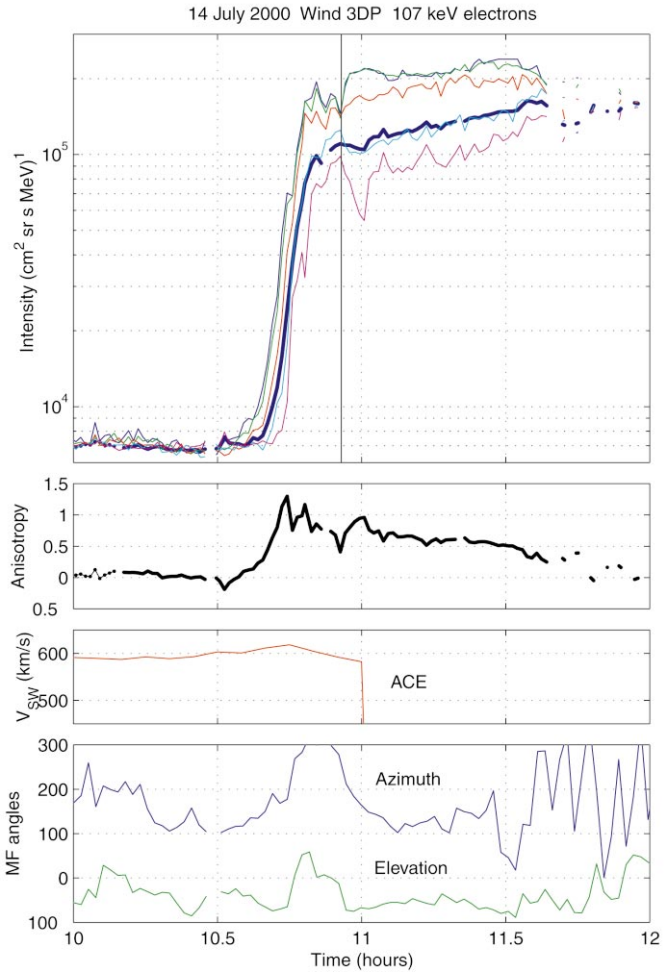

FIG. 6.—Particle and solar wind data for the 2000 July 14 solar event. The upper panel shows intensity profiles of *Wind* ~107 keV electrons at pitch angles of approximately 15°, 34°, 57°, 80°, and 100°, and the spin-averaged intensity (*thick line*). Subsequent panels show anisotropy profile, solar wind speed as observed on *ACE*, and *Wind* measurements of the magnetic field azimuth and elevation angles. Note that solar wind speed data are not available after ≈11:00 UT.

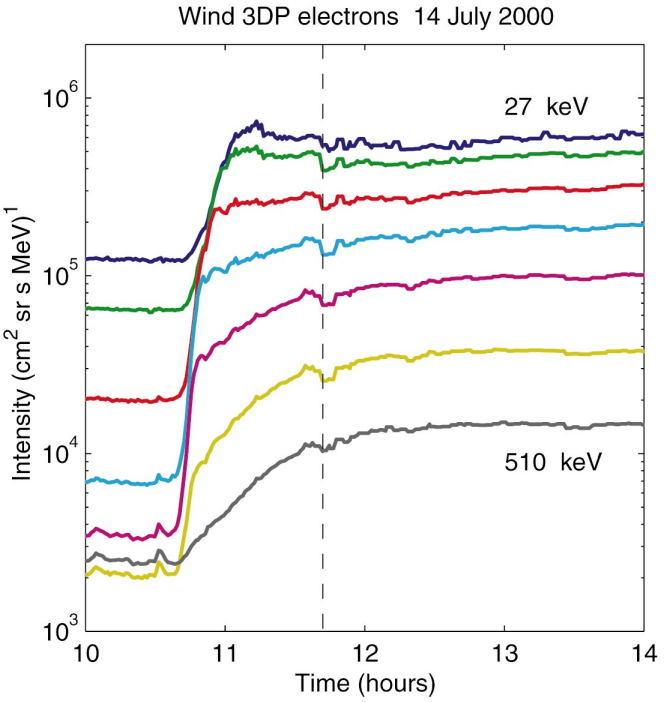

FIG. 7.—*Wind* 3DP electrons during the beginning of the 2000 July 14 solar event, observed in seven energy channels in the range 27–510 keV. After ~11:40 UT (*dashed line*) the data quality is affected by the high particle flux.

single orbit of these particles thus encompasses a distance corresponding to about 1 hr of solar wind flow. For this reason we chose to display a 1 hr moving average of the field, as higher time resolution data are not particularly relevant for these particles. For the same reason, we should not expect the flow vector to align exactly with the magnetic field. There is no reason that the magnetic field measured at a point should be the same as the average field sampled by the particle over its orbit, given that the Larmor radius is on the order of the coherence length of interplanetary magnetic turbulence.

2.2. *Solar Electrons*

The electron observations in the energy range ~20–500 keV analyzed in this work were made with the Three-dimensional Plasma and Energetic Particles (3DP) instrument aboard the *Wind* spacecraft (Lin et al. 1995). The 3DP instrument was designed to provide full three-dimensional coverage with 36° × 22.5 angular resolution. In the present work we use pitch-angle distributions (eight bins) with time resolution of 1 minute. During the onset of the particle event *Wind* was positioned at $X = -3$, $Y = -70$, and $Z = -6$ (GSE coordinates, units of Earth radii), outside of the Earth's magnetosphere.

Figure 6 shows the time history of ~107 keV electrons, together with *Wind* observations of the magnetic field azimuth and elevation angles, and the solar wind speed observed on the *ACE* spacecraft. Until ~10:55 UT, the onset of the electron flux exhibits the characteristics of a typical scatter-poor event: a rapid rise of electrons arriving from the Sun, and a delayed but noticeable flux of electrons scattered back from the antisunward direction, indicating weak but finite interplanetary scattering in the event. After 10:55 UT, the intensity starts to rise again, though at a much slower rate, and the anisotropy shows a second peak. Coincident with these features are drastic changes in the magnetic field azimuth and elevation angles, which might indicate a sudden transition of the spacecraft into a flux tube with different propagation conditions, or a different connection to the particle source close to the Sun. After 11:40 UT, the total particle flux reaches a level where reliable data recording was no longer possible. Plasma data from *ACE*, positioned at the Earth-Sun Lagrangian point, 240 Earth radii sunward of Earth, were affected by the intense particle fluxes even earlier.

Some clarification might be obtained by taking a look at the energy dependence of the features described above. Figure 7 shows the electron fluxes in seven energy bins, extending from 27 to 510 keV. It can be seen that at higher energies the intensity profiles remain flat after ~11:00 UT, or even continue to rise, although at a slower rate. This might indicate that a second injection of electrons took place that had a harder energy spectrum and occurred on a longer timescale. On the other hand, the dips in the anisotropy profiles (as will be shown later) do not show any time variation as a function of energy and are therefore probably a local effect.

3. MODELING

3.1. *Fits to Relativistic Solar Proton Data*

The intensity-time and anisotropy-time profiles of relativistic solar protons, derived from neutron monitor data as described in § 2.1, have been fitted by means of computer simulations of the interplanetary transport of solar energetic particles, followed by optimization of injection and transport parameters. In this work, we have subjected our fits to a particularly stringent test: a "double-blind" experiment in which different researchers independently performed fits using two sets of simulation and fitting techniques, referred to as models 1 and 2, which have both been previously employed to fit solar energetic particle data.

Though both models are based upon numerical solution of the Boltzmann equation, they have several differences in methodology as discussed below. Notably, they have quite different fitting philosophies (fitting "by eye" in model 1 and by χ^2 minimization in model 2). Each model was implemented without knowledge of parameters used for the other. The experiment was very successful in that the two models yielded quite similar results. We first discuss model 1, then model 2. However, to facilitate comparison, results from both models are shown together in the figures.

3.1.1. *Model 1*

The interplanetary magnetic field is described by a superposition of a smooth average field, represented by an Archimedean spiral, and a random or turbulent component. The motion of charged particles then has two corresponding components, adiabatic motion along the smooth field together with pitch-angle scattering by turbulence. Evolution of the particle phase space density $f(z, \mu, t)$ is given by a model of focused transport (Roelof 1969):

$$\frac{\partial f}{\partial t} + \mu v \frac{\partial f}{\partial z} + \frac{(1-\mu^2)}{2L} v \frac{\partial f}{\partial \mu} - \frac{\partial}{\partial \mu}\left(D_{\mu\mu}(\mu) \frac{\partial f}{\partial \mu}\right) = q(z, \mu, t), \quad (2)$$

where z is distance along the magnetic field line, $\mu = \cos\theta$ is the cosine of the particle pitch angle, and t is time. The particle velocity v remains constant in this model. The systematic forces are characterized by a focusing length $L(z)$ defined by $L^{-1} = -B^{-1}\partial B/\partial z$, where $B(z)$ is the diverging magnetic field, while the stochastic forces are described by a pitch-angle diffusion coefficient $D_{\mu\mu}(\mu)$. Injection of particles close to the Sun is given by $q(z, \mu, t)$.

If scattering is strong, $f(z, \mu, t)$ rapidly approaches isotropy. Particle transport can then be described by a diffusion-convection equation with a radial diffusion coefficient $K_r(r) = (1/3)\lambda_r v$, where λ_r is the radial mean free path. For solar particle transport, it is usually possible to neglect perpendicular diffusion, and the radial mean free path is then related to the parallel mean free path by $\lambda_r = \lambda_\parallel \cos^2\psi$, where ψ is the angle between the radial direction and the magnetic field. The parallel mean free path, $\lambda_\parallel$, is in turn governed by the pitch-angle diffusion coefficient (Hasselmann & Wibberenz 1968; Earl 1974):

$$\lambda_\parallel = \frac{3v}{8} \int_{-1}^{+1} d\mu \frac{(1-\mu^2)^2}{D_{\mu\mu}(\mu)}. \quad (3)$$

The mean free path is a convenient parameter for characterizing the varying degrees of scattering from one solar particle event to another, even in nondiffusive situations such as when the observer is less than one mean free path from the particle source.

The Bastille Day particle event was modeled with numerical solutions of equation (2) obtained with a finite-difference scheme (see Ng & Wong 1979; Schlüter 1985; Ruffolo 1991; Hatzky 1996). Mean free paths were derived by visually fitting the density and anisotropy predicted by the simulation with the density, n, and magnitude of first-order anisotropy, ξ, derived from observations (§ 2.1). Specifically, ξ was compared to the theoretical anisotropy A defined by

$$A(z, t) = \frac{3\int_{-1}^{+1} d\mu\mu f(z, \mu, t)}{\int_{-1}^{+1} d\mu f(z, \mu, t)}. \quad (4)$$

From the observed solar wind speed of 600 km s^{-1} the magnetic field spiral was mapped back to 0.05 AU, resulting in a nominal distance of $z = 1.07$ AU along the connecting field line that had its footpoint at N04° W36°.

The transport of particles away from the acceleration site and their subsequent injection onto the connecting field line at 0.05 AU were described phenomenologically by a Reid-Axford profile (Reid 1964)

$$Q_R(t) = \frac{C}{t} \exp\left\{-\frac{\tau_c}{t} - \frac{t}{\tau_L}\right\}, \quad (5)$$

where the rise and decay timescales τ_c and τ_L originally were envisioned to represent coronal diffusion from the flare and escape onto the connecting field line, respectively. We use this functional form to conveniently parameterize the source function in equation (2), but the actual transport does not need to be coronal diffusion. In fact, equation (5) can be regarded as a phenomenological representation of a generic injection process in which there is a fast rise to maximum, followed by a monotonic decay indicating injection close to the Sun over a finite amount of time. It can thus describe not only coronal diffusion but also enhanced scattering close to the Sun as well as particle acceleration in the higher corona (out to 0.05 AU).

The pitch-angle diffusion coefficient was assumed to be a separable function of z and μ,

$$D_{\mu\mu}(z, \mu) = \kappa_1(z)\kappa_2(\mu), \quad (6)$$

thereby permitting equation (3) to be rewritten as

$$\lambda_\parallel(z) = \frac{3v}{4\kappa_1(z)} \int_{-1}^{+1} d\mu \frac{(1-\mu^2)^2}{2\kappa_2(\mu)}. \quad (7)$$

The functional form of $\kappa_2(\mu)$ and hence of the pitch-angle dependence of $D_{\mu\mu}$ is shown in Figure 8. The normalization was chosen to make the integral in equation (7) equal to unity. This form of $\kappa_2(\mu)$ features reduced but finite scattering through $\mu = 0$, as predicted by current models of particle scattering (see Dröge 2000a, and references therein).

The only remaining assumption to be made concerns the spatial variation of $\kappa_1(z)$ or, equivalently, the mean free path. *Helios* observations of MeV electrons in the inner Heliosphere (Kallenrode, Wibberenz, & Hucke 1992) as well as multispacecraft studies (Beeck et al. 1987) indicate that a constant radial mean free path often provides a good fit of particle events. Accordingly, we assume that λ_r is spatially constant, which results in $\lambda_\parallel(z)$ increasing with z as the

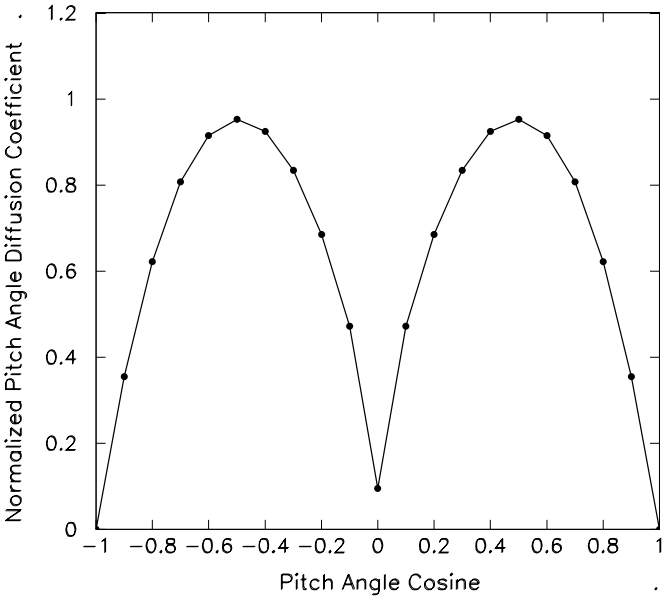

FIG. 8.—Pitch-angle dependence of the scattering coefficient $D_{\mu\mu}(\mu)$ assumed for model 1.

angle ψ increases with radial distance between 0.05 and 3 AU, the outer (free-escape) boundary of the simulation.

With the above assumptions, it was possible to obtain a good fit to the intensity-time profile of the neutron monitor data, with $\lambda_r = 0.1$ AU, $\tau_c = 0.1$ hr, and $\tau_L = 0.5$ hr, as shown by the blue curve in Figure 9. However, the fast decay of the anisotropy could not be modeled. We could, indeed, fit the high initial anisotropy by increasing the mean free path, but this would worsen the discrepancy later in the event. Correspondingly, a lower mean free path would worsen the discrepancy in the rise phase of the event.

A plausible explanation for the rapid isotropization of the near-Earth particle intensity would be the existence of a reflecting boundary, not too far downstream of Earth, which could be more efficient at scattering particles back than pitch-angle diffusion between 1 and 3 AU. Referring back to Figure 1, a large Forbush decrease occurred approximately 24 hr prior to the Bastille Day event and was still in progress at the onset of the Bastille Day particle event. The interplanetary disturbance associated with this Forbush decrease is a good candidate for providing the necessary reflecting boundary beyond Earth.

More detailed information about the nature of this disturbance can be gained from the behavior of the interplanetary magnetic field. As shown in Figure 10, a shock passed Earth around 10:00 UT on 2000 July 13, as evidenced by the fourfold increase in the magnetic field strength observed by both *ACE* and *Wind*. This was coincident with a jump in the solar wind speed from 500 to 700 km s^{-1} measured by *ACE*. By early morning of July 14, the magnetic field strength was back to its value before the arrival of the shock and the solar wind speed had dropped to 600 km s^{-1}. Another disturbance starting about 15:00 UT on July 14

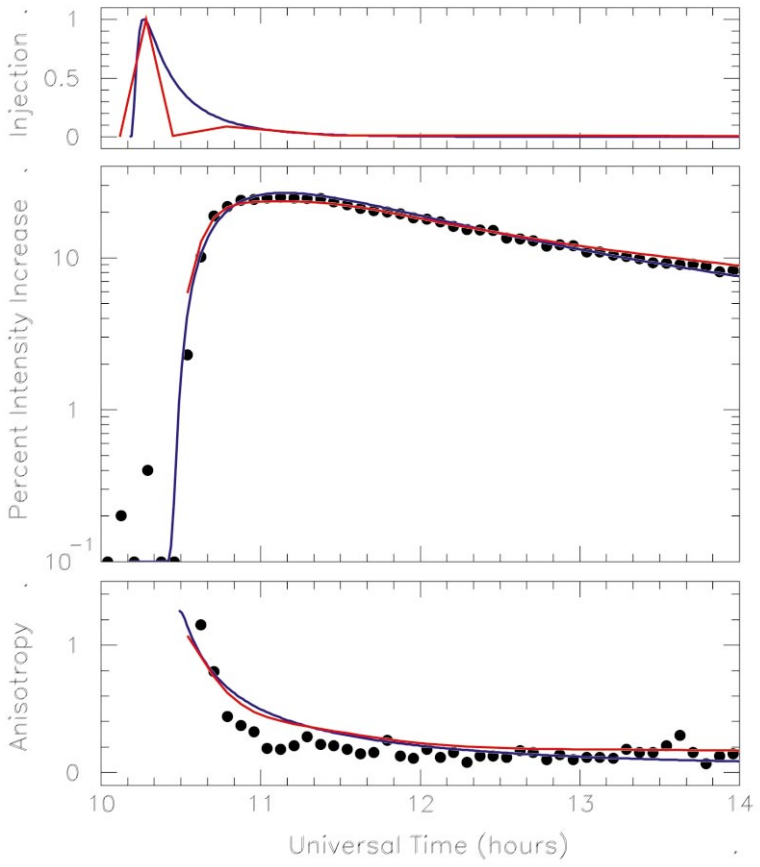

FIG. 9.—Modeling results with a standard Parker magnetic field. Data points are density (*middle*) and anisotropy (*bottom*) derived from neutron monitor data. Blue curves show the model 1 best fit, obtained with a radial mean free path $\lambda_r = 0.1$ AU. Red curves show model 2 best fit, obtained with $\lambda_r = 0.12$ AU. The upper panel shows the injection functions derived from the two models.

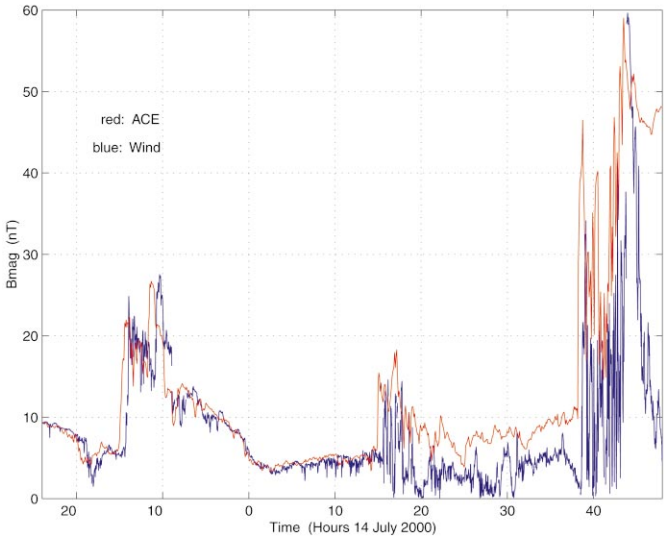

FIG. 10.—Magnitude of the interplanetary magnetic field observed on the *ACE* and *Wind* spacecraft during 2000 July 13–15.

may be related to a halo CME that was observed by the Large Angle and Spectrometric Coronagraph Experiment (LASCO) at 13:27 UT on July 11. The strong shock of the July 14 event reached Earth the following day at around ~15:00 UT. From the transit time of approximately 28 hr a mean propagation speed of 1500 km s^{-1} can be deduced for this shock.

The shock that passed Earth at 10:00 UT on July 13, and the following magnetic structures appear to have the properties required for a reflecting boundary. We therefore introduced a reflecting outer boundary at $r = 1.27$ AU, the estimated position of the center of the field enhancement at the onset time of the Bastille Day event. Different values of reflectivity were tried, and it was found that a reflectivity of 85% optimized the fit. Figure 11 shows the resulting fit (*blue curve*) to the intensity-time and anisotropy-time profiles of the neutron monitor data assuming $\lambda_r = 0.18$ AU, $\tau_c = 0.2$ hr, and $\tau_L = 0.3$ hr. For the parallel mean free path at 1 AU we find a value of $\lambda_{\parallel}(r) = \lambda_r(r)/\cos^2 \psi(r) = 0.27$ AU. Here we have taken the nominal angle between the radius vector and Archimedean field spiral for $V_{sw} = 600$ km s^{-1}, $\psi = 35°$, which is roughly consistent with the magnetic field observations.

It should be noted that the above fit was obtained for the median rigidity of the energetic solar protons causing the increase in the neutron monitor count rate, estimated to be 2.15 GV. However, the spread of rigidity in a "typical" solar cosmic-ray event at neutron monitor energies ranges from ~1 to 10 GV, and one might ask whether neglecting the corresponding velocity dispersion can affect the results of the fit. Additional simulations were made for 1 and for 10 GV, not changing the other parameters. The intensity-time and anisotropy-time profiles at 10 GV did not differ much

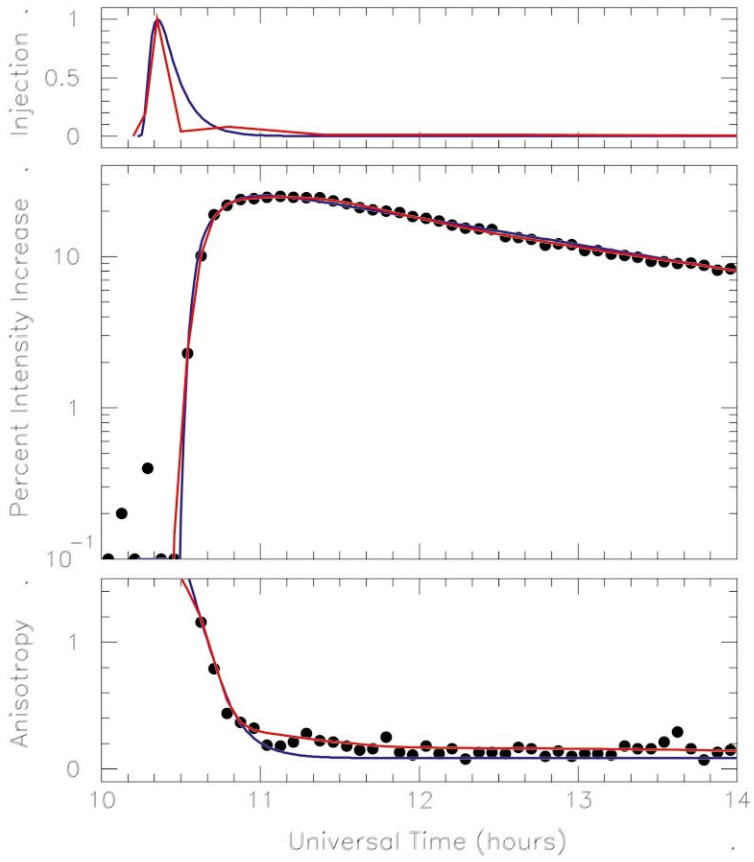

FIG. 11.—Modeling results with a magnetic barrier located beyond Earth. The format as in Fig. 9. Both model 1 (*blue*) and 2 (*red*) use a radial mean free path $\lambda_r = 0.18$ AU. The magnetic bottleneck has 85% reflectivity and is located at a heliocentric distance of 1.27 AU.

from the ones at 2.15 GV, whereas at 1 GV they were shifted in time by about 7 minutes. We find it reasonable to assume that the rise phase of the event is dominated by the greater than 2 GV protons and that the slower protons at most lead to a broadening of the maximum. The above value of $\lambda_{\parallel}$ should therefore be a good estimate for 2.15 GV protons. (Note also that model 2, described below, explicitly includes velocity dispersion and yields consistent results.)

Finally, we compare in Figure 12 the observed cosmic-ray pitch-angle distribution with that predicted by the simulation with the magnetic barrier. Each data point represents a 5 minute average count rate observed at an individual neutron monitor station. The "pitch angle" for a station was defined to be the angle between the symmetry axis (defined by the direction of the anisotropy vector) and the viewing direction of the station for a median rigidity solar particle (2.15 GV).

We consider the agreement between modeled and observed pitch-angle distributions to be remarkably good. It should be emphasized that the modeled distributions were exactly those obtained from fitting the intensity-time and anisotropy-time profiles, as described above. No additional free parameters were introduced to facilitate the comparison in Figure 12.

3.1.2. *Model 2*

In model 2, we use a finite difference method to solve an equation of pitch-angle transport, which in addition to streaming, focusing, and scattering as in equation (2) also considers adiabatic deceleration and solar wind convection (Ruffolo 1995, eq [11]). The injection is treated as an initial condition of particle density near the Sun. For the treatment of streaming and convection, a generalized total variation diminishing algorithm has recently been developed (Nutaro, Riyavong, & Ruffolo 2001). By implementing this in the present work, the simulation accuracy has been maintained while reducing the run time by a factor of 5: Δz has been increased fivefold, while other finite difference parameters and boundary conditions are as given by Ruffolo (1995).

For the pitch-angle scattering coefficient, we use the standard parameterization $A\,|\mu|^{q-1}(1-\mu^2)$ (Jokipii 1971) with $q = 1.5$, which is in the range of 1.3–1.7 inferred by Bieber et al. (1986). The resulting scattering coefficient is similar to that used in model 1 (Fig. 8). The value of A is set so as to achieve the user-specified value of $\lambda_{\parallel}$ in our finite difference representation of the transport problem (Ruffolo 1991). The radial mean free path is again taken to be independent of position for reasons described in § 3.1.1. The Compton-Getting transformation (Compton & Getting 1935) of the pitch-angle distribution from the solar wind frame, in which it is calculated, into Earth's reference frame has a negligible effect on the anisotropy for the relativistic particles considered here.

In the calculation of adiabatic deceleration, we assume a typical solar spectrum with a particle density $\propto p^{-5}$, where p is particle momentum. In order to represent the momentum distribution of the primary relativistic protons to which the neutron monitors are responding, we perform simulations for momentum values corresponding to the 5th, 15th, ..., 95th percentile rigidities described in § 2.1.2. Results for these 10 momentum values are averaged to determine the intensity and the weighted anisotropy expected near Earth, where "weighted anisotropy" is defined to be the product of intensity and the magnitude of anisotropy. However, when the final fit was repeated for a single momentum value (the 45th percentile), the results were essentially unchanged. A complete simulation takes about 24 minutes on a 450 MHz Pentium II computer.

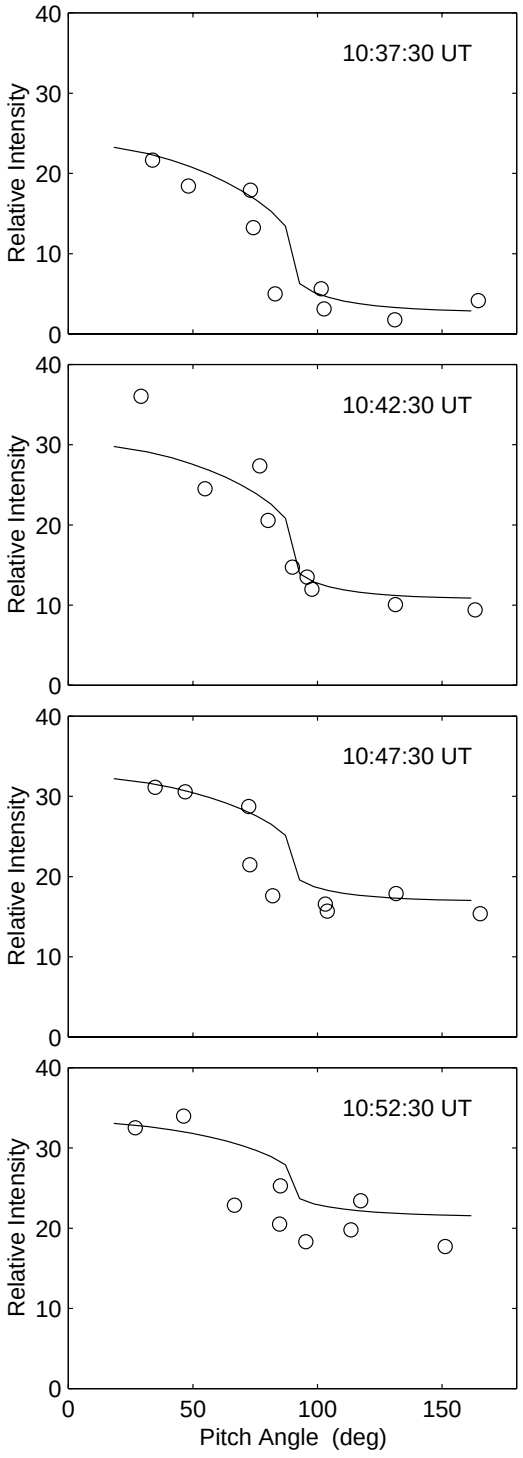

FIG. 12.—Model pitch-angle distributions (*lines*) are compared with 5 minute averaged neutron monitor count rates measured at individual stations (*circles*). The pitch angle corresponding to a station was computed using the median rigidity of response (2.15 GV).

The deconvolution of interplanetary transport effects from the neutron monitor measurements is carried out by a

piecewise linear fitting method, which has been successfully tested in comparison with fitting to a Reid-Axford profile (eq. [5]) for impulsive and gradual solar particle events (Ruffolo, Khumlumlert, & Youngdee 1998). We simultaneously fit data on the particle intensity versus time and the weighted anisotropy versus time, taking into account measurement uncertainties as estimated from preevent fluctuations. Fits are performed for a variety of λ_r values, with the optimal λ_r taken to be the one that minimizes the χ^2 value of the fit. We use the magnitude of the measured anisotropy (Fig. 5, *second panel*) because the anisotropy direction can fluctuate, not necessarily in tandem with fluctuations in the measured magnetic field, as discussed in § 2.1.3. The weighted anisotropy (anisotropy times intensity) is used instead of the anisotropy alone because the former is linear in the distribution function derived from a transport simulation, as required by the piecewise linear fitting method. (Note that apart from a factor of particle speed, v, the weighted anisotropy is proportional to the net streaming flux.) This method determines an optimal piecewise linear injection function (along with uncertainties) by linear least-squares fitting. The fitting procedure has recently been automated to truncate the injection function when it is inappropriately long (see Ruffolo et al. 1998), vary the start time, and expand or contract the injection function. Advantages of this inversion technique include its complete objectivity, speed, ease of use, ability to treat narrow injection pulses, and flexibility in approximating general functional forms. The technique can fail if the transport model is inappropriate, i.e., giving results inconsistent with the data, a problem not encountered in the present analysis.

The best fit to the relativistic solar protons observed on Bastille Day based on these techniques is shown in Figure 9 (*red curves*). We used a fitting interval from 10:00 to 15:00 UT, though in fact the optimized parameters are very strongly influenced by the early phase of the event, where the most rapid variations occur. The injection function of particles released near the Sun has a peak at 10:18:30 UT and a FWHM of 5 minutes. This is similar to the peak time of the X-ray flare at the Sun, 10:16 UT (or 10:24 UT as observed near Earth), given that the data are in 5 minute intervals. There is good agreement with results from model 1, including a similar injection profile and virtually the same derived scattering mean free path, $\lambda_r = 0.12$ AU. (This fit gave a χ^2 value of 361 for 111 degrees of freedom [dof].) However, from either model one can conclude that the rapid drop in the anisotropy cannot be explained by a standard picture of interplanetary transport.

The magnetic field data presented in Figure 10 suggest an explanation of the rapidly decreasing anisotropy in terms of magnetic mirroring. The data indicate a magnetic "bottleneck," i.e., a localized constriction of the magnetic field lines, which at the time of interest was located approximately 1.3 AU from the Sun, just downstream of an interplanetary shock. As mentioned in § 3.1.1, this shock passed Earth around 10:00 UT on July 13.

The parent solar event was identified with the help of on-line data from the Space Environment Center[2] and *ACE* Science Center.[3] Most CME-driven interplanetary shocks arrive 3–4 days after the CME, though this time can be shorter for a fast event. Type II and IV radio bursts and long-duration X-ray events are known to be associated with interplanetary shocks (e.g., Cane & Stone 1984).

The major solar event of July 14 occurred in active region 9077 at N22° W07°, and this same region dominated solar activity on previous days as well. The only solar event during July 9–11 from which both type II radio emission and X-ray emission were observed was the event with an X-ray peak at 21:42 UT on July 10 and Hα emission at N18° E49°. This event, also from region 9077, produced long-duration (>1 hr) X-ray emission of intensity M5.7 as well as type II and IV radio bursts. Considering *ACE*/SIS data for ions of ≈3–30 MeV nucleon^{-1}, a nondispersive onset of ion fluxes began late on July 10, followed by a gradual, energy-independent increase typical for ions accelerated at a traveling interplanetary shock, until a peak on July 13 near the time when the interplanetary shock passed *ACE*. This provides the most convincing evidence for an identification of the interplanetary shock of July 13 with the E49 solar event at 21:42 UT on July 10.

Figure 13 illustrates the likely configuration of the interplanetary magnetic field at the time of the July 14 event. CME ejecta from the July 10 event, located at longitude E49 with respect to Earth, drove an interplanetary shock and compressed magnetic field lines at their western edge, as observed near Earth on July 13. Solar particles emitted near the Sun on July 14 would mostly be reflected by this magnetic bottleneck. More specifically, the process of magnetic mirroring (also known as adiabatic focusing) approximately conserves the magnetic moment (first adiabatic invariant), $p_\perp^2/(2meB)$, thus conserving $(1 - \mu^2)/B$, where μ is the cosine of the pitch angle. In the absence of scattering, the minimum value of μ for which particles could pass through the bottleneck would be $R = (1 - 1/r)^{1/2}$, where r is the maximum magnetic compression. Conversely, particles with $0 < \mu < R$ would not penetrate the magnetic bottleneck. Then R can be interpreted as a reflection coefficient, because in a near steady state the distribution function would be nearly uniform (isotropic) in μ, and this value

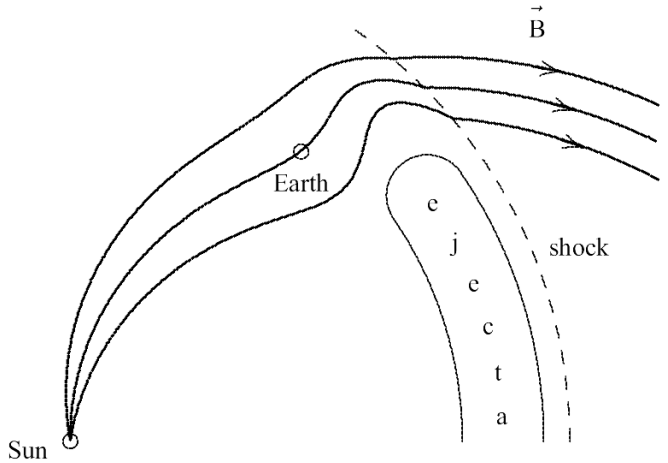

FIG. 13.—Schematic configuration of the interplanetary magnetic field at the time of the solar flare/CME of 2000 July 14. A previous flare/CME event from the same active region on 2000 July 10, then at 49° east longitude, led to the interplanetary shock and magnetic compression observed near Earth, which was at the western side of the CME ejecta. The neutron monitor data provide strong evidence for the reflection of relativistic solar protons from this magnetic bottleneck.

[2] See http://solar.sec.noaa.gov.
[3] See http://www.srl.caltech.edu/ACE/ASC.

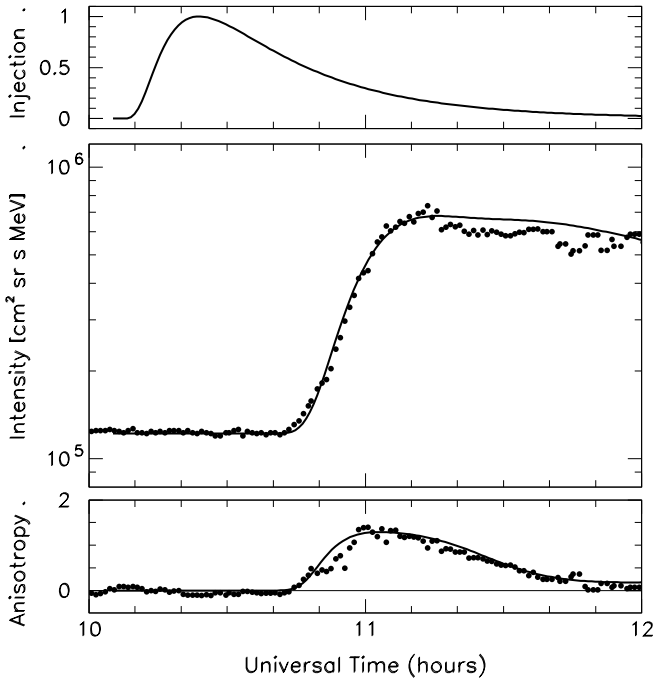

FIG. 14.—Fits to the electron intensity-time and anisotropy-time profiles of 27 keV electrons observed on *Wind* after the 2000 July 14, 10:24 UT flare, assuming a constant $\lambda_r = 0.5$ AU.

would represent the fraction of particles reflected by magnetic mirroring. In the present case, the magnetic compression ratio was ≈ 4, corresponding to a reflection coefficient of ≈ 0.87.

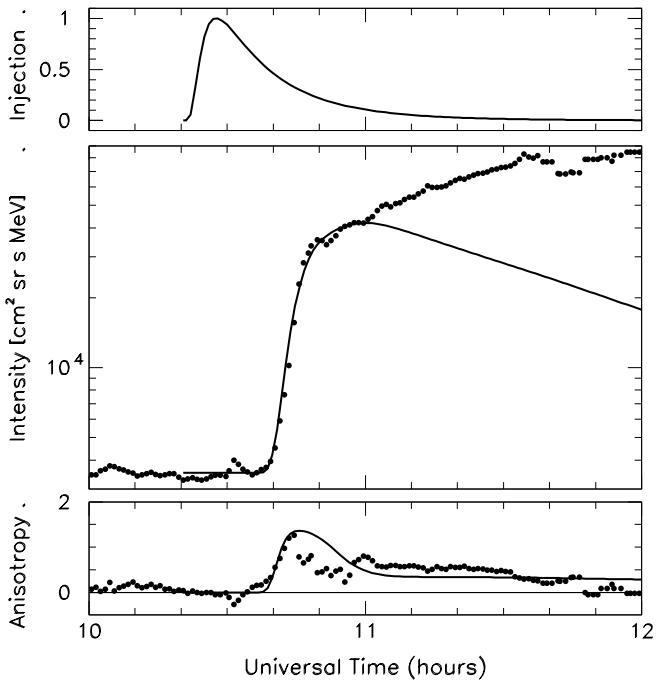

FIG. 15.—Fits to the electron intensity-time and anisotropy-time profiles of 179 keV electrons observed on *Wind* after the 2000 July 14, 10:24 UT flare, assuming a constant $\lambda_r = 0.36$ AU.

The magnetic bottleneck has a nontrivial effect on the particle transport. For example, the first particles arriving at a given location (e.g., at the bottleneck) are highly anisotropic because these are particles that have undergone unusually little scattering and are moving almost directly outward along the interplanetary magnetic field, i.e., with $\mu \approx 1$; a large fraction of these particles will actually pass through the bottleneck. Furthermore, this is not merely a "leaky box," with rapid equilibration within the bottleneck followed by slow leakage through it. In fact, "leakage" through the bottleneck is typically rapid, a fraction of the particles outside can penetrate back in, and detailed simulations show that the omnidirectional intensity near Earth is hardly affected by the bottleneck, which mainly dams the outflow of particles in its immediate vicinity. However, the anisotropy at Earth is substantially affected, with the bottleneck indeed helping to explain the relativistic proton data.

To take the above effects into account, we modify the transport equation of Ruffolo (1995) for a magnetic bottleneck located within the simulation region. Although in principle a change in the curvature of the magnetic field lines requires changing and adding terms to the transport equation (see Skilling 1971; Isenberg 1997; Kóta & Jokipii 1997; Ruffolo & Chuychai 1999), such changes are of order (solar wind speed)/(particle speed) and are weak for relativistic particles, with the exception of the change to the focusing term that we consider here. For computational convenience, we still relate z, the arclength along the mean magnetic field, to r as for an Archimedean spiral, and consider a compression in $(\ln B)$ of Gaussian form:

$$\ln B = (\ln B)_{\rm Arch} + \eta \exp\left[-\frac{(r-r_0)^2}{2\sigma^2}\right],$$

$$\frac{1}{L} = -\frac{d}{dz}\ln B$$

$$= \left(\frac{1}{L}\right)_{\rm Arch} + \eta \cos\psi \, \frac{r-r_0}{\sigma^2}$$

$$\times \exp\left[-\frac{(r-r_0)^2}{2\sigma^2}\right], \qquad (8)$$

where "Arch" refers to values for an uncompressed Archimedean spiral field; r_0 is heliocentric distance at the center of the bottleneck; ψ is the "garden-hose" angle between $\hat{r}$ and $\hat{z}$; σ is a measure of the width of the bottleneck, taken to be 0.05 AU; and the amplitude η is chosen so that the discrete sum of focusing occurring at each grid point corresponds to the desired reflection coefficient, R. This represents the first treatment of focused transport for a magnetic bottleneck inside the simulation region.

We first set r_0 to 1.3 AU, the bottleneck location estimated from magnetic field data (Fig. 10). These simulations indeed provided a much better fit, in particular to the rapidly declining anisotropy. We then explored what values of the reflection coefficient and scattering mean free path would best fit the data, as a test of whether the inferred properties of the bottleneck were consistent with the magnetic field measurements. The best fit was for $R = 0.8$, close to the value expected from the magnetic field data, providing further evidence for the explanation of mirroring associated with this magnetic field structure. This fit had a χ^2 value of 179 for 110 dof, $\lambda_r = 0.13$ AU ($\lambda_\parallel = 0.19$ AU), an

injection peak at 10:19 UT, and an injection FWHM of 5 minutes.

Finally, another fit to the relativistic solar proton intensity and weighted anisotropy was performed for the same parameters as used in the final fit with model 1: $r_0 = 1.27$ AU, $R = 0.85$, and $\lambda_r = 0.18$ AU ($\lambda_{\|} = 0.27$ AU). The results, shown in Figure 11 (*red curves*), had an improved χ^2 of 162, again for 109 dof. The best-fit piecewise linear injection profile implies a single peak at 10:21 UT with a FWHM of 7 minutes. This injection width is somewhat narrower than that obtained for model 1, but the difference is less than the 5 minute resolution of the observations. Overall, the excellent fit to the neutron monitor data provides strong evidence for the reflection of relativistic solar protons from a magnetic bottleneck beyond Earth.

3.2. *Fits to Solar Electron Data*

Model 1 was used to simulate the supposed first injection of electrons observed on *Wind*, until about 11:00 UT, with similar boundary conditions as the neutron monitor data except for allowing different λ_r values and injection profiles for different energy ranges. We have assumed that the dip in the anisotropy profiles from $\sim$10:45 to 10:57 UT was due to a local effect and tried to optimize the modeling of the intensities and anisotropies until 11:00 UT. Because of complications from this local effect and the possible second injection, it is difficult to draw conclusions from electron data about the reflecting boundary beyond Earth. However, the electrons do provide information on scattering conditions between the Sun and Earth.

Figure 14 shows the best fit to the 27 keV electrons under these restrictions, obtained with $\lambda_r = 0.5$ AU, $\tau_c = 0.4$ hr, and $\tau_L = 0.7$ hr. For the parallel mean free path of the electrons at 1 AU we find a value of $\lambda_{\|} = 0.75$ AU. The simulation models the data well during the rise phase of the event until 11:00 UT or so. Because the useful data extend only to 11:40 UT we have not attempted to model a possible second injection. A fit to the *Wind* 179 keV electrons is shown in Figure 15, obtained with $\lambda_r = 0.36$ AU ($\lambda_{\|} = 0.54$ AU), $\tau_c = 0.16$ hr, and $\tau_L = 0.33$ hr.

4. DISCUSSION AND CONCLUSIONS

A principal result of this work is that transport of relativistic solar cosmic rays during the Bastille Day event (2000 July 14) was strongly influenced by a magnetic mirror or reflecting boundary located some 0.3 AU beyond Earth. A notable feature of the Bastille Day event was the very rapid decrease from an initially high value of anisotropy. Transport models using a conventional Parker magnetic field were unable to produce a satisfactory fit to this feature, but revised models that included a reflecting magnetic field structure beyond Earth yielded an excellent fit to time profiles of both the intensity and anisotropy.

Concurrent *ACE* and *Wind* measurements of the magnetic field provide additional support for this scenario. A strong ($\sim$4 times) enhancement of the magnetic field magnitude was observed approximately 20 hr prior to onset of the Bastille Day event. The field enhancement was related to a prior CME shock that also produced a Forbush decrease. The expected location and reflection coefficient of this field enhancement are excellent matches with the properties inferred from modeling the cosmic rays.

Evidence for magnetic mirroring of relativistic solar protons has been presented previously (e.g., Cramp et al. 1997). In fact, the configuration shown in Figure 13 may not be particularly unusual; it merely requires that the same active region produced a CME-driven interplanetary shock a few days earlier, when it was in a more easterly location. In such a case Earth may well be located near the western margin of the CME ejecta, where magnetic field lines are compressed as illustrated in the figure.

An ability to include magnetic mirroring in transport codes improves the reliability and accuracy of the ordinary mean free path resulting from scattering by turbulence. Our initial modeling with a Parker field yielded a best-fit parallel mean free path of 0.15 AU. Adding a magnetic mirror improved the fit dramatically, but the best-fit mean free path nearly doubled, to a value of 0.27 AU. In a certain sense, then, the magnetic mirror was contributing approximately half the total amount of scattering affecting cosmic rays on Bastille Day 2000.

We also modeled low-energy electrons observed by *Wind*. The derived parallel mean free paths are 0.75 AU at 0.17 MV (energy of 27 keV) and 0.54 AU at 0.46 MV (energy of 179 keV). Remarkably, low-energy electron mean free paths are larger than relativistic proton mean free paths at 10,000 times higher rigidity ($\sim$2 GV).

This result is consistent with the observation by Dröge (2000b) that the rigidity dependence of the mean free path changes surprisingly little from event to event, even though the level of scattering in the interplanetary medium varies greatly. Plotted versus rigidity, the mean free path displays a broad minimum at intermediate rigidities and rises both for low-rigidity electrons and for high-rigidity protons. Such a rigidity dependence is predicted in recent theoretical treatments that combine effects of a turbulence dissipation range with effects of dynamical turbulence or wave damping (Bieber et al. 1994; Schlickeiser 1994).

A feature of the present analysis has been the use of two independent transport simulations to model the data. Very similar results were obtained from models 1 and 2, which employ somewhat different methods to simulate solar injection and magnetic mirroring, and which also employ different fitting techniques. Model 1 uses the traditional method of fitting by eye, with an emphasis on the very early phase of the event. Model 2 involves automated, objective fitting to minimize a χ^2 value. While in principle this gives equal weight to each data point, in practice the very early points again strongly constrain the fit, because simulations with an inappropriate λ_r or injection profile tend to grossly misfit these points. Our double-blind test has shown that these very different fitting philosophies can yield nearly identical results, giving one greater confidence in both methods.

We believe that the simulation described in § 3.1.2 above (model 2) is the first implementation of automated χ^2 fitting in a state-of-the-art solar particle transport code. Further development of such methods may permit near real-time characterization of interplanetary transport parameters, for use in making space weather forecasts of radiation intensities and fluences in solar energetic particle events.

Neutron monitors of the Bartol Research Institute are supported by NSF grant ATM 00-00315. Additional support was provided by NASA grants NAG 5-7142 and NAG 5-8134. This work was also supported by a Basic Research Grant from the Thailand Research Fund. We thank J. Clem, J. Roth, L. Shulman, and C.-H. Tsao for their contributions to the Bartol neutron monitor program.

We thank R. P. Lin for helpful discussions. For contributing neutron monitor data, we thank our colleagues at IZMIRAN (Russia), the Polar Geophysical Institute (Russia), the Australian Antarctic Division and University of Tasmania, Potchefstroom University (South Africa), and the French Polar Institute and Paris-Meudon Observatory. We thank N. F. Ness and D. J. McComas for providing *ACE* magnetic field and plasma data via the *ACE* Science Center.

REFERENCES

Beeck, J., Mason, G. M., Hamilton, D. C., Wibberenz, G., Kunow, H., Hovestadt, D., & Klecker, B. 1987, ApJ, 322, 1052
Bieber, J. W., & Evenson, P. 1991, Proc. 22d Int. Cosmic-Ray Conf. (Dublin), 3, 129
———. 1995, Proc. 24th Int. Cosmic-Ray Conf. (Rome), 4, 1316
———. 1998, Geophys. Res. Lett., 25, 2955
Bieber, J. W., Evenson, P. A., & Pomerantz, M. A. 1986, J. Geophys. Res., 91, 8713
Bieber, J. W., Matthaeus, W. H., Smith, C. W., Wanner, W., Kallenrode, M.-B., & Wibberenz, G. 1994, ApJ, 420, 294
Cane, H. V., & Stone, R. G. 1984, ApJ, 282, 339
Compton, A. H., & Getting, I. A. 1935, Phys. Rev., 47, 817
Cramp, J. L., Duldig, M. L., Flückiger, E. O., Humble, J. E., Shea, M. A., & Smart, D. F. 1997, J. Geophys. Res., 102, 24237
Debrunner, H., Flückiger, E., Grädel, H., Lockwood, J. A., & McGuire, R. E. 1988, J. Geophys. Res., 93, 7206
Dröge, W. 2000a, Space Sci. Rev., 93, 121
———. 2000b, ApJ, 537, 1073
Duggal, S. P. 1979, Rev. Geophys., 17, 1021
Duggal, S. P., & Pomerantz, M. A. 1976, J. Geophys. Res., 81, 5032
Earl, J. A. 1974, ApJ, 193, 231
Hasselmann, K., & Wibberenz, G. 1968, Z. Geophys., 34, 353
Hatzky, R. 1996, Ph.D. thesis, Univ. Kiel
Isenberg, P. A. 1997, J. Geophys. Res., 102, 4719
Jokipii, J. R. 1971, Rev. Geophys. Space Phys., 9, 27
Kallenrode, M.-B., Wibberenz, G., & Hucke, S. 1992, ApJ, 394, 351
Kóta, J., & Jokipii, J. R. 1997, Proc. 25th Int. Cosmic-Ray Conf. (Durban), 1, 213
Lin, R. P., et al. 1995, Space Sci. Rev., 71, 125
Lin, Z., Bieber, J. W., & Evenson, P. 1995, J. Geophys. Res., 100, 23,543
Lockwood, J. A. 1971, Space Sci. Rev., 12, 658
Nagashima, K., & Fujimoto, K. 1993, Proc. 23d Int. Cosmic-Ray Conf. (Calgary), 3, 719
Ng, C. K., & Wong, K. Y. 1979, Proc. 16th Int. Cosmic-Ray Conf. (Kyoto), 5, 252
Nutaro, T., Riyavong, S., & Ruffolo, D. 2001, Comput. Phys. Commun., 134, 209
Reid, G. C. 1964, J. Geophys. Res., 69, 2659
Roelof, E. C. 1969, in Lectures in High Energy Astrophysics, ed. H. Ögelmann & J. R. Wayland (NASA SP-199; Washington, DC: NASA), 111
Ruffolo, D. 1991, ApJ, 382, 688
———. 1995, ApJ, 442, 861
Ruffolo, D., & Chuychai, P. 1999, Proc. 26th Int. Cosmic-Ray Conf. (Salt Lake City), 6, 552
Ruffolo, D., Khumlumlert, T., & Youngdee, W. 1998, J. Geophys. Res., 103, 20591
Schlickeiser, R. 1994, ApJS, 90, 929
Schlüter, W. 1985, Ph.D. thesis, Univ. Kiel
Shea, M. A., Smart, D. F., Wilson, M. D., & Flückiger, E. O. 1991, Geophys. Res. Lett., 18, 829
Skilling, J. 1971, ApJ, 170, 265
Stoker, P. H. 1985, Proc. 19th Int. Cosmic-Ray Conf. (La Jolla), 4, 114